Angular dependence of metamagnetic transitions in $DyAgSb_2$

K. D. Myers and P. C. Canfield
Ames Laboratory and Department of Physics and Astronomy, Iowa State University, Ames, Iowa 50010

V. A. Kalatsky and V. L. Pokrovsky
Department of Physics, Texas A&M University, College Station, Texas 77843

(Received 19 August 1998)

Measurements of the magnetization of $DyAgSb_2$ reveal a complex system of up to 11 well-defined metamagnetic states for the field applied within the basal plane. Measurements of the magnetization vs the angle the applied field makes with respect to the [110] axis show the Dy^{3+} moments are constrained to lie along one of the four [110] directions within the basal plane. From the angular dependence of the critical fields and plateau magnetizations, the net distribution of the moments may be deduced for each state. Finally, the coupling constants are calculated within the framework of the ''four-position clock model.'' [S0163-1829(99)04302-7]

INTRODUCTION

Recent studies of $HoNi_2B_2C$ and other RNi_2B_2C compounds have shown that the net distribution of magnetic moments in a metamagnetic system may be determined from the analysis of the angular dependence of the magnetization and transition fields of the metamagnetic states.[1–3] Although no information about the wave vector associated with the metamagnetic ordering may be obtained, this approach allows a vast amount of information to be gained about the metamagnetic phases, without requiring neutron or magnetic x-ray diffraction.

In $HoNi_2B_2C$, a strong crystalline electric field (CEF) anisotropy constrains the local moments to the [110] crystallographic axes, leading to four well-defined metamagnetic states with relatively simple angular dependence. This angular dependence suggests that the net distribution of magnetic moments may be described by $\uparrow\downarrow$ for $H<H_{c1}$, $\uparrow\uparrow\downarrow$ for $H_{c1}<H<H_{c2}$, $\uparrow\uparrow\rightarrow$ for $H_{c2}<H<H_{c3}$, and $\uparrow\uparrow\uparrow$ for $H>H_{c3}$, where $\uparrow$ and $\rightarrow$ correspond to the moment directed either along or perpendicular to the [110] axis nearest to the field and H_{ci} are the four angular-dependent critical fields. Recent theoretical work[2] has analyzed these data within the framework of the ''four-position clock model,'' where the local moments are restricted to either the $\langle 110\rangle$ or $\langle 100\rangle$ sets of axes by a strong CEF anisotropy.

To further understand this type of planar metamagnetism, we have undertaken a search for other systems that have rare-earth ions in locations with tetragonal point symmetry. Although the RSb_2 series with R=Ce, Pr, and Nd is strongly anisotropic and exhibits sharp well-defined metamagnetic states for the field applied within the *ab* plane,[4] the crystal structure is weakly orthorhombic,[5,6] which greatly complicates the analysis of the magnetic structure. In contrast to the RSb_2 series of compounds, $RAgSb_2$ crystallizes in the simple tetragonal $ZrCuSi_2$ structure ($P4/nmm$, # 129)[7–9] consisting of Sb-RSb-Ag-RSb-Sb layers with the R^{3+} in a location with tetragonal point symmetry (4 mm).

Measurements of the magnetization as a function of applied field along high-symmetry axes in $DyAgSb_2$ revealed a series of four sharp steps in the magnetization for the field applied within the basal plane, making the compound a potential candidate for further study of the angular dependence of metamagnetic states. In addition, hysteresis is only present in two of the transitions, simplifying the analysis.

In this paper, we present a study of the angular dependence of the metamagnetic transitions of $DyAgSb_2$. After an overview of the experimental techniques used to grow and characterize the samples, results and plausible model of the net distribution of magnetic moments will be presented. Finally, the angular dependencies of the critical fields will be used to deduce the coupling parameters within the framework of the four-position clock model.

EXPERIMENTAL METHODS

High-quality single crystals of $DyAgSb_2$ were flux grown[10] from an initial composition of $Dy_{0.045}Ag_{0.091}Sb_{0.864}$. Essentially, this Sb-rich self-flux was chosen because of its low-melting temperature and because it introduces no new elements into the melt. The additional silver content also helps to preclude formation of DySb. The constituent elements were placed in alumina crucibles and sealed in quartz under a partial argon pressure. The starting materials were heated to 1200 °C, and then cooled to 670 °C over 120 h. Removal of the flux revealed platelike crystals with typical dimensions of $3\times3\times1$ mm. The *c* axis was perpendicular to the plate. The sample exhibited well-defined facets, corresponding to [100] and [110] edges, as determined by x-ray diffraction using a rotating anode source (Mo Kα, $\lambda=0.71069$ Å) and four circle diffractometer. For the rest of this paper, all angles will be relative to [110]. The residual resistivity ratio $[RRR=R(300\text{ K})/R(2\text{ K})]$ of 40 is consistent with low impurity and dislocation concentrations.

Magnetic measurements were performed in a Quantum Design superconducting quantum interference device magnetometer with a specially modified sample holder to rotate the sample, keeping the *c* axis perpendicular to the field. A sample mass below 0.5 mg was used to avoid torque on the rotator due to the extreme magnetic anisotropy. To reduce the effects of weighing errors, M(H) data were collected on a 10.62 mg sample from the same batch, for H$\|$[100] and

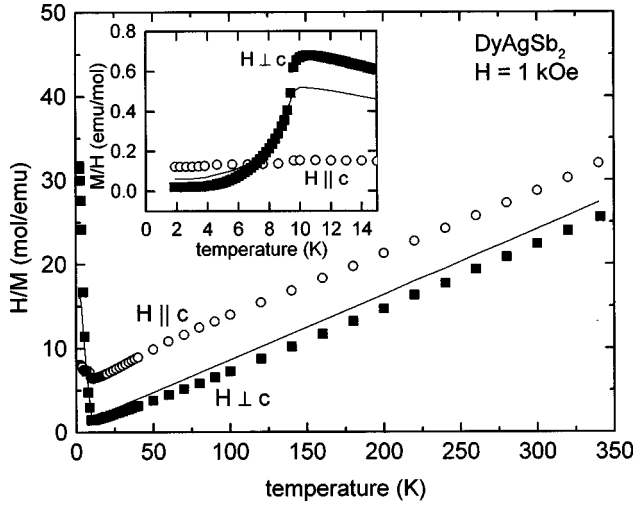

FIG. 1. Applied field divided by magnetization (H/M) for $H\|c$ (○) $H\perp c$ (■) and polycrystalline average (solid line) vs temperature for $DyAgSb_2$. Inset: low-temperature behavior of magnetization divided by field for $H\|c$ (○) $H\perp c$ (■), and polycrystalline average (solid line).

[110]. The data from the small sample were then normalized to the larger sample data. Angular uncertainty in the rotator is estimated to be less than 1°. Additional uncertainty in the sample orientation could arise from a failure to align the c axis of the sample exactly perpendicular to the applied field. However, due to the construction of the sample holder, this misalignment should be no more than 10°.

EXPERIMENTAL RESULTS

The inverse susceptibility (Fig. 1) of $DyAgSb_2$ illustrates the strong anisotropy, with the local Dy moments aligning within the basal plane. Above 100 K, the inverse susceptibilities are linear, allowing fits to the Curie-Weiss law. The polycrystalline average, determined by $(2\chi_{H\perp c}+\chi_{H\|c})/3$, yields an effective moment of 10.3 μ_B/Dy and a Weiss temperature of −10.1 K. Anisotropic Weiss temperatures are −86.3 K for $H\|c$ and 7.1 K for $H\perp c$. The inset to Fig. 1 clearly shows that magnetic ordering is present below 9 K, with the susceptibility for $H\perp c$ rapidly decreasing below 9 K.

In order to better understand the nature of the ordering below 9 K, magnetization as a function of applied field was measured at 2 K for H parallel to the c axis and for H parallel to [100] and [110], shown in Fig. 2. For the applied field along the c axis, the magnetization is linear, only reaching about 1.6 μ_B/Dy at 55 kOe. However, for the applied field in the basal plane, four well-defined metamagnetic states and the low-field antiferromagnetic state are observed, with the transition fields and the plateau magnetizations varying strongly with the angle of the applied field. At 55 kOe, M for H‖[110] is slightly less than 10 μ_B/Dy while for H‖[100] M is approximately 7.2 μ_B/Dy. This is consistent with the easy magnetic axis being along the ⟨110⟩ directions. In addition, some of the field-induced magnetic transitions exhibit field up/field down hysteresis. In particular, the higher field kneelike states (M_3 and M_6) persist for a greater range of fields as the magnitude of the applied field is decreased.

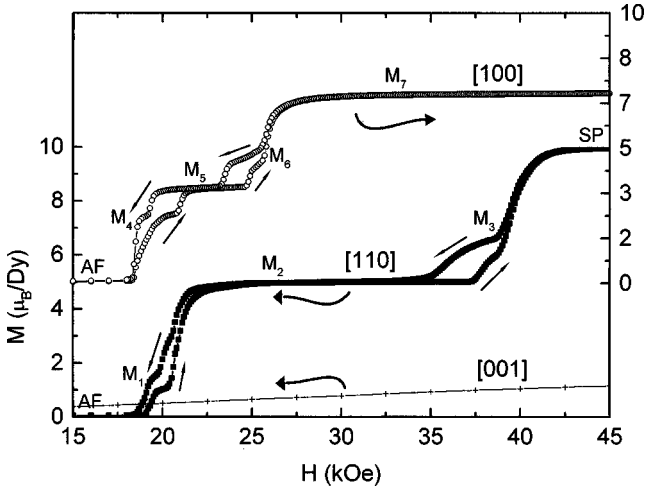

FIG. 2. $M(H,T=2\,\mathrm{K})$ for increasing and decreasing field for the field applied along [001] (+, left axis), [110] (■, left axis), and [100] (○, right axis). Note: the offset zero on the right axis.

Although the range of stability of the kneelike states M_1, M_3, M_4, and M_6 is quite small, the fact that they exist in both the field up and field down data leads to the conclusion that they are stable states rather than just metastable, transitional states. As a further test of the stability of these metamagnetic phases, the following experiment was performed. After cooling to 2 K in zero field, M(H) for H‖[110] was measured with increasing field up to 19.7 kOe, entering the kneelike M_1 plateau, as shown in Fig. 3. Maintaining 19.7 kOe, the temperature was then increased up to 12 K, well above the ordering temperature of 9.5 K, and then decreased back to 2 K (inset Fig. 3.) Finally, M(H) was measured for fields greater than 19.7 kOe. These data are consistent with M_1 being thermodynamically stable for this applied field, since the moments would have minimized the energy after the ''anneal,'' by settling into the lowest energy state for the

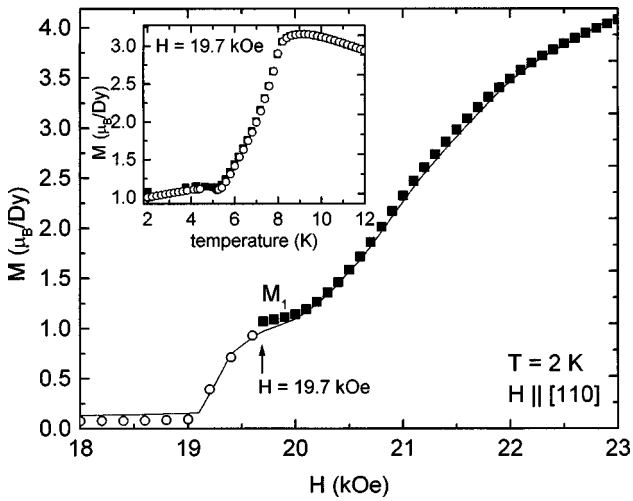

FIG. 3. Detail of M(H) for H‖[110] for the M_1 state. Solid line is $M(H)$ at 2 K zero-field cooled, Open circles (○) are for zero-field cooled magnetic isotherm up to 19.7 kOe. Squares (■) are magnetic isotherm for the sample cooled to 2 K from 12 K in a 19.7 kOe field. Note: the plateau at 19.7 kOe is stabilized by field cooling. Inset: $M(T)$ in 19.7 kOe for increasing (○) and decreasing temperature (■).

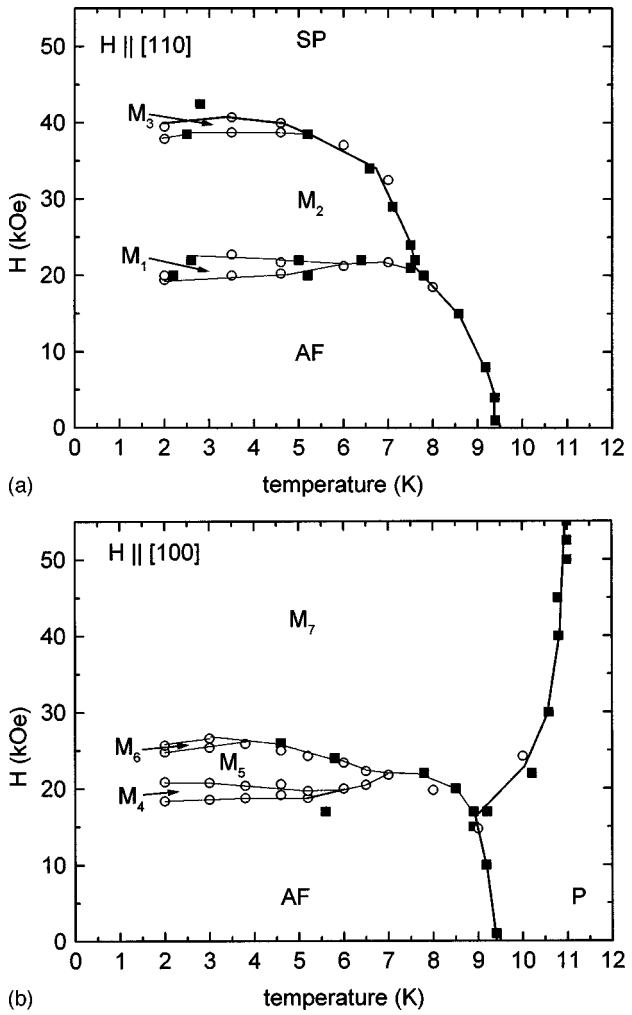

FIG. 4. Applied field-temperature phase diagrams for (a) H||[110]. (b) H||[100]. Points are determined from $M(T)$ (■) and $M(H)$ (○).

given magnitude and orientation of the magnetic field. By analogy, it is assumed that the M_3, M_4, and M_6 are also stable states.

Figures 4(a) and 4(b) show the temperature-applied field phase diagrams for H parallel to [110] and [100], respectively. The points were determined from the local maxima in dM/dH (shown by ○) from M(H) field-increasing scans at selected temperatures and dM/dT (shown by ■) from M(T) scans at selected fields. Both phase diagrams are qualitatively similar at low temperatures, with the kneelike phases M_1, M_3, and M_6 persisting up to approximately 6 K, and the other metamagnetic states persisting up to about 8 K. However, an additional phase boundary is evident between 9.5 and 11 K in the H||[100] phase diagram, separating the M_7 metamagnetic state and the paramagnetic region. The lack of this upper transition in the H||[110] phase diagram, combined with the fact that $M(55\ \text{kOe}) \approx 10\ \mu_B/\text{Dy}$, suggests that the high-field, low-temperature state may simply be a saturated paramagnet state.

To study the angular dependence of the metamagnetic states, it is important to first determine the single-ion anisotropy associated with the CEF splitting of the Hund's rule ground state J multiplet. To measure this, crystals of $YAgSb_2$ were grown with a small amount of Dy introduced

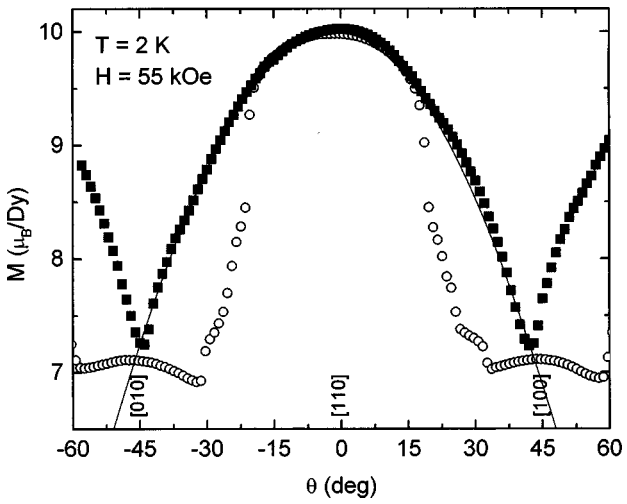

FIG. 5. $M(\theta)$ at $H = 55$ kOe for $DyAgSb_2$ (○) and $Dy_{0.07}Y_{0.93}AgSb_2$ (■). Solid line is $M_{sat} = 10\ \mu_B \cos(\theta)$.

into the melt. From the Curie-Weiss effective moment and the saturated magnetic moment, the crystals were determined to be $Dy_{0.07}Y_{0.93}AgSb_2$. Magnetization vs angle measurements in a 55 kOe field at 2 K for both $DyAgSb_2$ and $Dy_{0.07}Y_{0.93}AgSb_2$ (Fig. 5) show that the dilute case closely follows a $M \propto \cos(\theta)$ dependence (shown by solid line). Since only the component of the magnetization parallel to the field is measured, this is consistent with the local Dy^{3+} moments being constrained to the nearest easy, [110], axis within the basal plane. Although fourfold symmetry is also observed in the $M(\theta)$ scans of $DyAgSb_2$, large deviations from $M \propto \cos(\theta)$ are readily apparent, where interactions between local moments [deviations from $\cos(\theta)$] and hysteresis [asymmetry of $M(\theta)$ curves] affect the magnetization. These data are consistent with a number of metamagnetic states crossing 55 kOe at different angles.

Magnetization isotherms are shown in Figs. 6(a)–6(c) for a series of angles relative to the easy [110] axis, divided into three angular regions for clarity. In region I ($\theta < 10°$), five different states are observed. Below 19 kOe, the compound orders in the antiferromagnetic (AF) state. As the field increases, a small kneelike state (M_1) is followed by a well-defined plateau (M_2) with a saturated moment near $5\ \mu_B/\text{Dy}$. Above 38 kOe, another kneelike state (M_3) is followed by a final plateau, corresponding to the saturated paramagnetic (SP) state with a moment close to the full-saturated moment, $g_J J \mu_B$, of the Hund's rule ground state of $10\ \mu_B/\text{Dy}$.

For angles between 10 and 25° (region II), the magnetization isotherms become more complex, with as many as seven metamagnetic states appearing, depending on the angle of the applied field. Many of these states are present for limited field and angular ranges, sometimes only appearing as inflection points with no clear plateaus in the magnetization.

When the angle increases above 25° (region III), the magnetization isotherms become similar to Region I, with the low-field AF state and two large steps (M_5 and M_7) each preceded by a kneelike step (M_4 and M_6). In this case, however, the maximum value for the magnetization in the

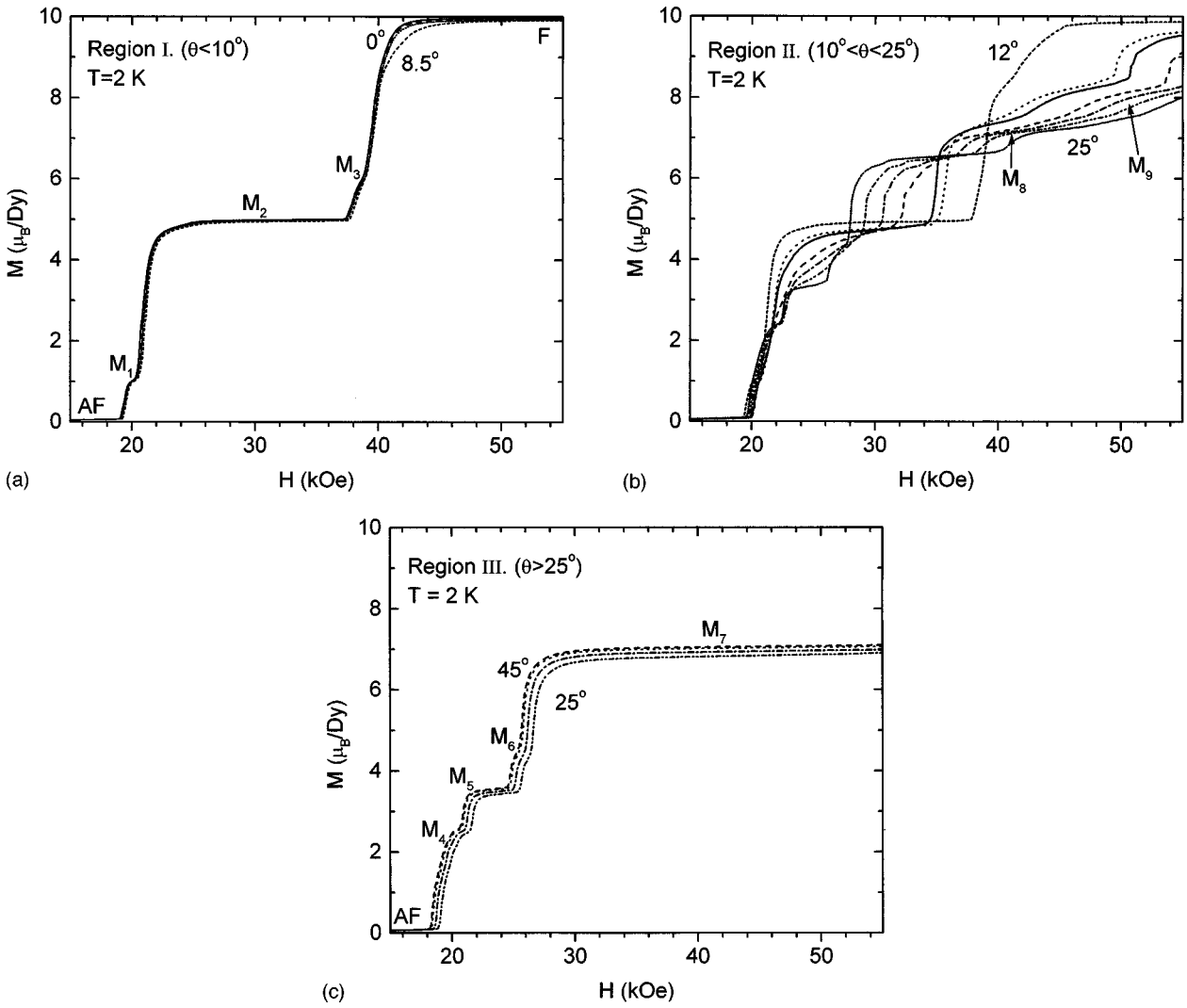

FIG. 6. Magnetization (M) vs applied field (H) at 2 K for a variety of angles relative to the easy axis, [110]. (a) angles (θ) less than 10° (b) angles between 10° and 25°, (c) angles between 25 and 45°.

highest-field state (M_7) approaches only about 7.2 μ_B/Dy as seen in Fig. 6(c).

From the magnetization isotherms [Figs. 6(a)–6(c)], the critical fields (H_c) and saturation magnetizations (M_{sat}) may be determined for each state as a function of angle, shown in Figs. 7(a) and 7(b), respectively. When possible, the saturated magnetic moment (M_{sat}) was determined by the magnetization, $M(H)$, midway between the bordering transition fields (shown by ● in the figure). For the highest-field states, M_{sat} was simply determined by the magnetization at the highest field attained (55 kOe).

The critical fields, determined from local maxima in dM/dH, are shown in Fig. 7(b). For transitions at angles between 12 and 25°, the peaks in dM/dH were frequently broad and poorly defined, particularly for the higher-field states. Consequently, no meaningful direct fit to an angular function could be made (see below).

From the magnetization isotherms shown in Figs. 6(a)–6(c) and the angular dependence of the critical fields and saturated moments [Figs. 7(a) and 7(b)], it is natural to divide the analysis into three regions. Within region I, the critical fields of the four states (two large steps, and two knees) are a minimum at $\theta = 0°$ and increase slightly as the angle increases. The solid lines in this region are fits to $H_c(\theta) = H_c/\cos(\theta)$ with $H_{cAF,1} = 19.4$, $H_{c1,2} = 20.6$, $H_{c2,3} = 37.8$, and $H_{c3,4} = 39.4$ kOe, where $H_{cAF,1}$ denotes the critical field between the AF and M_1 states. The saturated moments of these states are all a maximum at 0° and decrease as the angle increases. The solid lines in the figure show fits to $M_{sat} = M_{sat}\cos(\theta)$ with $M_{sat1} = 1.0$, $M_{sat2} = 5.0$, $M_{sat3} = 5.8$, and $M_{sat4} = 10.0\ \mu_B$/Dy.

In Region III, the critical fields of the four transitions are all minimized at 45°. Fits (shown by solid line) show that $H_c(\theta) = H_c/\cos(45° - \theta)$ with $H_{cAF,4} = 18.4$, $H_{c4,5} = 20.9$, $H_{c5,6} = 24.8$, and $H_{c6,7} = 25.7$ kOe. Likewise, the saturated moments are maximized at 45° and vary as $M_{sat}\cos(45° - \theta)$ with $M_{sat4} = 2.6$, $M_{sat5} = 3.5$, $M_{sat6} = 4.5$, and $M_{sat7} = 7.2\ \mu_B$/Dy.

EXPERIMENTAL DATA ANALYSIS

Despite the complexity of the metamagnetism presented in this system, it is possible to create a consistent model of the net distribution of the magnetic moments. To facilitate this, we introduce the four-position clock model.[2] This model arises from a strong CEF anisotropy restricting the

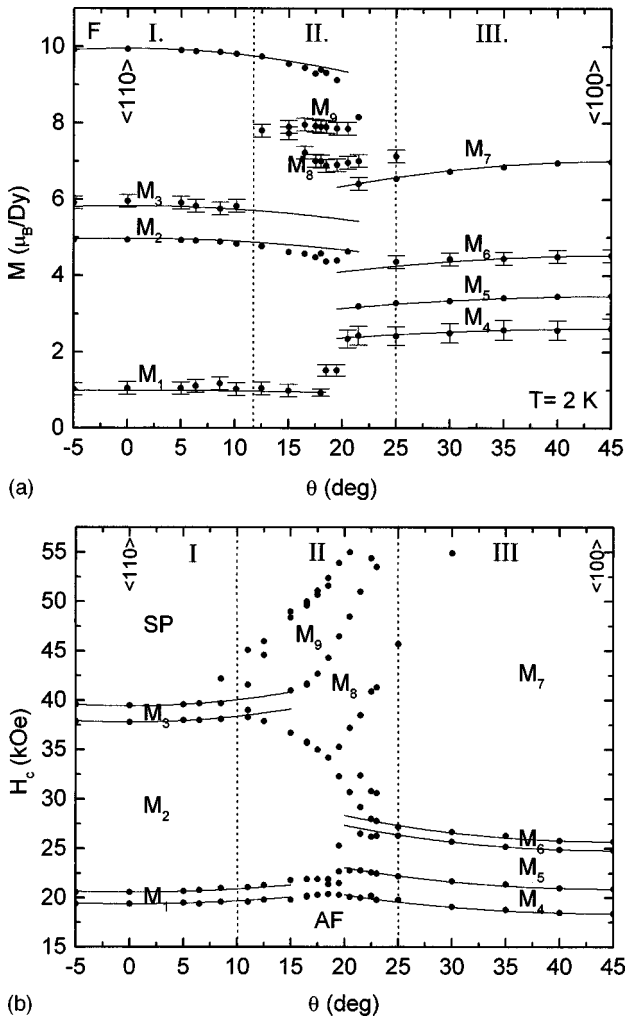

FIG. 7. Angular dependence of (a) saturated moment ($M_{\rm sat}$) and (b) critical field (H_c) using criteria described in text. Solid lines are fits to the data.

local moments to lie along one of four crystallographically similar orientations within the basal plane given by $\uparrow$, $\leftarrow$, $\downarrow$, $\rightarrow$, or angles relative to the nearest easy $\langle 110\rangle$ axis (0, 90, 180, or 270°).

Within this model, the net distribution of the local moments may be determined from the angular dependence of the critical fields and saturated moments of the metamagnetic states.[1] Since the magnetometer measures only the projection of the magnetic moment along the applied field, the angular dependence of the magnetization of an arbitrary state is given simply by:

$$M_{\rm Sat}(\theta)=\frac{M}{N}\sum_i \cos(\theta-\phi_i),$$

where θ is a continuous variable expressing the orientation of the applied field and ϕ_i is a discrete variable denoting the orientation of the ith moment relative to the easy axis, free to take values of 0, 90, 180, or 270°. N is the number of moments needed to describe the state, and M is the saturated moment of the free Dy^{3+} ion in the CEF split ground state. Therefore, when $M_{\rm sat}(\theta)\propto\cos(\theta)$, all of the moments are aligned parallel to the closest easy axis or are cancelled out by antiparallel moments (e.g., $\uparrow\uparrow\uparrow\downarrow$ or $\uparrow\uparrow\uparrow\uparrow$). However, when $M_{\rm sat}\propto\cos(45°-\theta)$, an equal number of moments are directed along the two nearest easy orientations with the rest of the moments canceling each other (e.g., $\uparrow\downarrow\uparrow\rightarrow$, $\uparrow\rightarrow$) since, $\cos(\theta)+\cos(90°-\theta)=\sqrt{2}\cos(45°-\theta)$. It should be noted that it is impossible to determine from magnetic measurements whether canceling antiparallel pairs of moments consist of $\uparrow\downarrow$ or $\leftarrow\rightarrow$. For simplicity, $\uparrow\downarrow$ will be used to denote a pair of canceling moments.

Regions of the data in Fig. 5 are consistent with the two extremes described above. For the isolated Dy ion in the $Dy_{0.07}Y_{0.93}AgSb_2$ pseudoternary the moment is always along the nearest easy [110] axis. For the concentrated $DyAgSb_2$, in which the Dy moments are ordered at low temperature, for $-15°<\theta<15°$ the moments have a behavior consistent with the saturated paramagnetic state. On the other hand, for $30°<\theta<60°$, $M(\theta)$ follows $\cos(\theta-45°)$, consistent with an ordered structure with a net distribution of moments $\uparrow\rightarrow$.

An equally simple argument may be used to determine the angular dependence of the critical fields. Since the energy due to a moment in a magnetic field is just $H\cdot M$, the difference in energy to due to application of the magnetic field between two different metamagnetic states (consisting of N_1 moments with orientations ϕ_{i1} and N_2 moments with orientations ϕ_{i2}) is simply:

$$\Delta E_{2,1}=\frac{HM}{N_2}\sum_i^{N_2}[\cos(\theta-\phi_{i2})]-\frac{HM}{N_1}\sum_i^{N_1}[\cos(\theta-\phi_{i1})].$$

If a critical energy ($E_{\rm Crit}$) exists, which must be exceeded to induce the next higher metamagnetic state, then the critical field will be given by:

$$H_{c2,1}(\theta)=\frac{E_{\rm Crit}}{\frac{1}{N_2}\Sigma_i^{N_2}[\cos(\theta-\phi_{i2})]-\frac{1}{N_1}\Sigma_i^{N_1}[\cos(\theta-\phi_{i1})]}.$$

In principle, $E_{\rm Crit}$ may be taken as a constant for a given transition since it depends only on the differences in the coupling between the two metamagnetic states. Therefore, the angular dependence of the critical fields may be used to gain insight into the net distribution of moments of the metamagnetic phases without *a priori* knowledge of the details of the ordering. For example, the critical field for a transition from $\uparrow\downarrow$ (AF) to $\uparrow\downarrow\uparrow\uparrow$ (M_2) (i.e., a flip of one spin from $\downarrow$ to $\uparrow$) will be proportional to $1/\cos(\theta)$ while a transition from $\uparrow\downarrow$ (AF) to $\uparrow\downarrow\uparrow\rightarrow$ (M_5) (i.e., a flip of one spin from $\downarrow$ to $\rightarrow$) will be proportional to $1/\cos(45°-\theta)$.

It is now possible to assign net distribution of moments for each of the metamagnetic states. For the two large plateaus within region I (M_2 and SP), the saturated moment as a function of angle closely follows $M_{\rm sat}\cos(\theta)$, suggesting that all of the moments are either canceled by an antiparallel moment ($\uparrow\downarrow$) or lie along the nearest axis to the field ($\uparrow$). Since the magnetization for state SP corresponds to the saturated moment for Dy^{3+}, all of the moments must be parallel giving a net distribution of moments of $\uparrow$. The saturated moment of M_2 is near 5 μ_B/Dy, consistent with half of the moments canceling and half aligned parallel to 0° giving $\uparrow\downarrow\uparrow\uparrow$. Since the two kneelike states (M_1 and M_3) are stable for a very limited range of fields, an accurate determination of the saturated moment is difficult. However, Fig. 7(a)

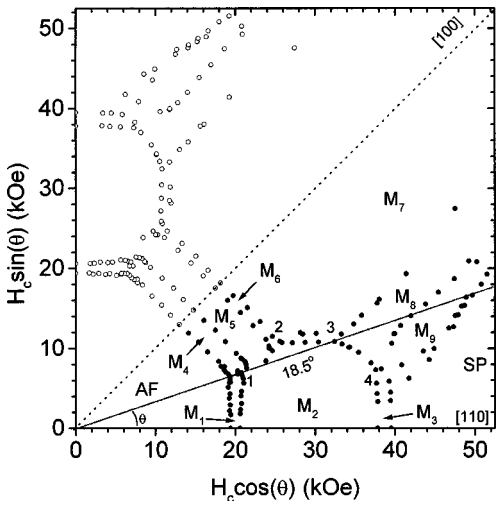

FIG. 8. Polar plot of the critical fields (H_c) with the metamagnetic phases labeled. Labels 1–4 represent the critical points used in the determination of the coupling constants as described in text. Note: points in upper left (○) were determined from a reflection of the measured data (●) across the [100] axis.

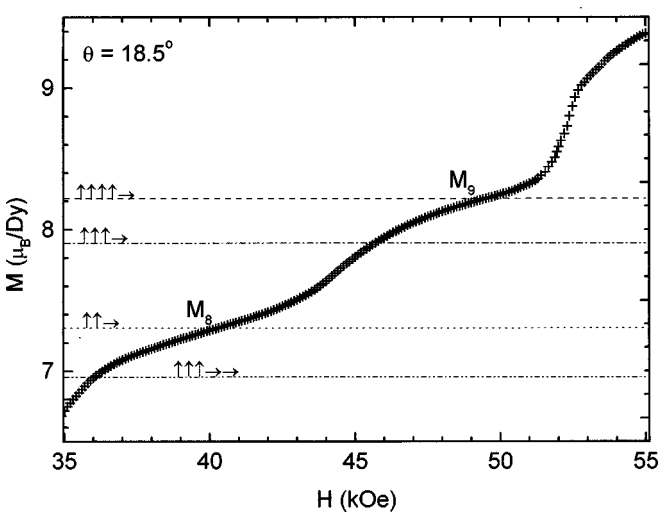

FIG. 9. Detail of M(H) for $\theta = 18.5°$ showing the magnetization of the M_8 and M_9 states. Lines represent calculated magnetization for the possible net distributions of moments (given by arrows) at 18.5°.

shows the angular dependence of M_{sat} for these states is consistent with $M_{\text{sat}}\cos(\theta)$ with $M_{\text{sat1}} \approx 1.0\mu_B$/Dy and $M_{\text{sat3}} \approx 5.8\ \mu_B$/Dy. From these estimates, a possible net distribution of moments for M_1 is ↑↑↓↑↓↑↓↑↓, although other distributions with a larger number of moments cannot be dismissed. Likewise, the magnetization of M_3 corresponds to ↑↑↑↑↓. The angular dependence of the critical fields within region I is consistent with the net distribution of moments for these four states since for all of the transitions, $H_c(\theta) \propto H_c\cos(\theta)$, which is expected for a moment (or multiple moments) flipping from ↓ to ↑.

In region III, the analysis is similarly straightforward. For all of the states, $M_{\text{sat}}(\theta) \propto M_{\text{sat}}\cos(45° - \theta)$ and $H_c(\theta) \propto H_c/\cos(45° - \theta)$. This behavior is consistent with an equal number of unpaired moments parallel and perpendicular to the nearest easy axis (↑→). Starting with M_7, we see that maximum magnetization is about 7.2 μ_B/Dy, corresponding to ↑→, since 7.2 μ_B/Dy ≈ 10 μ_B/Dy cos(45°). Likewise, the plateau magnetization of M_5 is 3.5 μ_B/Dy, close to half of M_7, indicating that half of the moments cancel, yielding a net distribution of moments of ↑↓↑→. Analysis of the two kneelike states within this region M_4 and M_6 also show similar angular behavior. From the magnetization of these states, possible net distributions of moments are consistent with ↑↓↑↓↑→ for M_4 and ↑→↑→↑↓ for M_6. The angular dependencies of the critical fields corroborate these assignments, since $H_c(\theta) \propto H_c/\cos(45° - \theta)$ for a change from ↓ to →.

Now that a plausible model for the states in regions I and III has been presented, we can turn the analysis to region II. Within this region (Fig. 7), many states exist for extremely limited range of fields and angles, greatly complicating the analysis. Furthermore, two new states appear at high fields, M_8 and M_9. This situation is simplified if a polar plot of the critical fields is made (Fig. 8). From the polar plot, it becomes clear that many of the transitions observed in region II arise from the $M(H)$ scan crossing a corner of a larger region of phase space, as shown by the line representing the M(H) scan at 18.5°.

TABLE I. Energies of metamagnetic states.

State	Energy of the state
AF (↑↓)	$-K_1+K_2-K_3+L_1+L_2+L_3$
SP (↑)	$K_1+K_2+K_3+L_1+L_2+L_3-h_x$
↑→	$K_2-L_1+L_2-L_3-1/2(h_x+h_y)$
↑↑↓	$-(K_1+K_2)/3+K_3+L_1+L_2+L_3-h_x/3$
↑↑→	$(K_1+K_2+3K_3-L_1-L_2+3L_3-2h_x-h_y)/3$
↑↑↑↓	$L_1+L_2+L_3-h_x/2$
↑↑↑→	$(K_1+K_2+K_3)/2-(3h_x+h_y)/4$
↑↑↓→	$-K_2/2-(h_x+h_y)/4$
↑↓↑→	$-(K_1-K_2+K_3)/2-(h_x+h_y)/4$
↑↑↑↑↓	$(K_1+K_2+K_3)/5+L_1+L_2+L_3-3h_x/5$
↑↑↓↑↓	$-(3K_1-K_2-K_3)/5+L_1+L_2+L_3-h_x/5$
↑↑→↑→	$(K_1+3K_2+3K_3-3L_1+L_2+L_3-3h_x-2h_y)/5$
↑↑↑↑↑↓	$(K_1+K_2+K_3)/3+L_1+L_2+L_3-2h_x/3$
↑↓↑→←→	$-(2K_1-K_2-L_1+L_2)/3-L_3-(h_x+h_y)/6$

TABLE II. Net distributions of moments for all of the observed metamagnetic states and the measured angular dependence of the saturated moment for each state.

State	Net Moments	$M_{\text{sat}}(\theta)$ (μ_B)
AF	↑↓↑↓	0
F	↑↑↑↑	10.0 cos(θ)
M_1	↑↓↑↓↑↓↑↓↑	1.0 cos(θ)
M_2	↑↓↑↑	5.0 cos(θ)
M_3	↑↓↑↑↑	5.8 cos(θ)
M_4	↑↓↑↓↑→	2.6 cos(θ−45°)
M_5	↑↓↑→	3.5 cos(θ−45°)
M_6	↑↓↑→↑→	4.5 cos(θ−45°)
M_7	↑→↑→	7.2 cos(θ−45°)
M_8	↑↑↑→	7.0±0.3
M_9	↑↑↑↑→	7.8±0.3

In the polar plot, the angular dependencies of all of the transitions becomes clear, particularly critical fields involving the two states existing only in region II. As seen in Fig. 8, four types of transitions are observed, each possessing linear phase boundaries, but with slopes in the polar plot of either 0, ∞, $+1$, or -1. Since the general equation of a straight line (with slope m and y intercept b) on a polar plot is given by $R(\theta)=b/(\sin\theta+m\cos\theta)$, the angular dependence of H_c may easily be deduced from the polar plot. Within the lower-right half of the phase diagram, the slopes, angular dependencies, and change in net distribution of moments are given by:

$m=0$	$H_c(\theta)\propto H_c/\sin\theta$	$\leftarrow$ to $\rightarrow$
$m=\infty$	$H_c(\theta)\propto H_c/\cos\theta$	$\downarrow$ to $\uparrow$
$m=+1$	$H_c(\theta)\propto H_c/\sin(45°-\theta)$	$\rightarrow$ to $\uparrow$
$m=-1$	$H_c(\theta)\propto H_c/\cos(45°-\theta)$	$\downarrow$ to $\rightarrow$

This is consistent with the transitions previously discussed. Furthermore, since $H_{C7,8}$ (the critical field between states M_7 and M_8), $H_{C8,9}$, and $H_{C9,SP}$ all exhibit slopes of near unity in the polar plot, these transitions correspond to flips of one moment from $\rightarrow$ to $\uparrow$. It should also be noted that deviations from linearity or a slope deviating from the aforementioned ones may indicate more complex transitions.

With the net distributions of moments of M_7 known to be $\uparrow\rightarrow$ and SP known to be $\uparrow$, it follows that M_8 and M_9 will then consist only of a number of $\uparrow$ moments and a smaller number of $\rightarrow$ moments. The next step then is to determine this distribution. Unfortunately, considerably larger slopes are present in the magnetizations of the M_8 and M_9 states, making an accurate determination of the saturated moment difficult. Figure 9 shows an expansion of a selected $M(H)$ scan in this region with the calculated magnetization of some of the possible distributions of moments. If the midpoint of the magnetization plateau, between the neighboring critical fields, is used, the magnetization suggests that the net distribution of moments of M_8 and M_9 are likely given by $\uparrow\uparrow\rightarrow$ and $\uparrow\uparrow\uparrow\uparrow\rightarrow$, respectively. However, other distributions containing larger numbers of moments cannot be ruled out.

A more detailed investigation into the nature of the magnetic order for each of the metamagnetic phases is possible, now that a consistent model for the net distribution of moments for each state has been determined. Within the ''four-position clock model,'' the Hamiltonian of an arbitrary magnetic state Φ consisting of moments ϕ_i may be obtained by an extension of the anisotropic next-nearest neighbor Ising (ANNNI) model, to include four possible directions instead of two and interactions with more than the next-nearest neighbors. We introduce the general spin-chain Hamiltonian with interactions between all spins:

$$\mathcal{H}(\Phi)=\sum_{n=1}^{\infty}\sum_{i=-\infty}^{\infty}[K_n\cos(\phi_i-\phi_{i+n}) + L_n\cos 2(\phi_i-\phi_{i+n})] - h_x\sum_{i=-\infty}^{\infty}\cos\phi_i - h_y\sum_{i=-\infty}^{\infty}\sin\phi_i,$$

where K_n and L_n are coupling constants, ϕ_i represents the angular orientation of the moment (constrained to only 0, 90, 180, or 270° by the CEF) of ion i, and h_x and h_y are the x and y components of the applied field, respectively. As written, the Hamiltonian includes all spins, since the summation on n runs from 1 to infinity. With up to 3rd nearest-neighbor interactions, stable phases are calculated with periods up to six moments, with Table I listing the energies of some of these metamagnetic states. For the transition from metamagnetic state Φ_1 to Φ_2, the critical field may then be given by:

$$H_{c2,1}(\theta,\Phi_1,\Phi_2)=\frac{\Sigma_{n=1}^{3}\Sigma_{i=-\infty}^{\infty}\{K_n[\cos(\phi_{i,2}-\phi_{i+n,2})-\cos(\phi_{i,1}-\phi_{i+n,1})]+L_n[\cos 2(\phi_{i,2}-\phi_{i+n,2})-\cos 2(\phi_{i,1}-\phi_{i+n,1})]\}}{\Sigma_{i=-\infty}^{\infty}[\cos(\theta-\phi_{i2})-\cos(\theta-\phi_{i1})]},$$

where the numerator is the energy that must be overcome E_{Crit} to stabilize the new state, as discussed previously.

Once the net distribution of moments for each state is determined, summarized in Table II, it is possible to calculate the coupling coefficients K_n and L_n in the Hamiltonian. To do this, it is helpful to return to the polar plot of H_c (Fig. 8). Here, the angular dependencies are more readily seen, especially for the intermediate angles (region II). The following series of equalities and an inequality may also be acquired from the triple points in the phase diagram, labeled 1–4 in the lower right half of the diagram.

$$\begin{aligned}
h_{1x}&=2(K_1-K_2+K_3)=20\ \text{kOe} & h_{1y}&=-4(L_1+L_2+L_3)=7\ \text{kOe}\\
h_{2x}&=2(K_1+K_3)+4L_2=24\ \text{kOe} & h_{2y}&=2K_2-4(L_1+L_3)=11\ \text{kOe}\\
h_{3x}&=2(K_1+K_3)-4L_2=34\ \text{kOe} & h_{3y}&=h_{2y}\\
h_{4x}&=2(K_1+K_2+K_3)=38\ \text{kOe} & h_{4y}&=h_{1y}
\end{aligned}$$

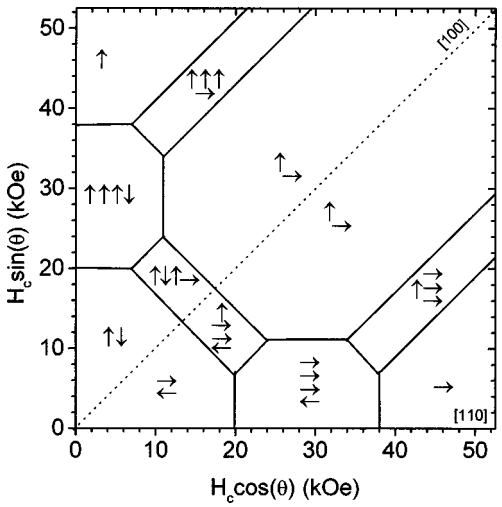

FIG. 10. Phase diagram determined from calculated-coupling constants. Arrows represent net distributions of moments for each of the metamagnetic states and point in the actual direction of the magnetic moment.

In addition, since the $\uparrow\uparrow\downarrow$ state does not appear in the phase diagram, its energy must be greater than that for the $\uparrow\uparrow\uparrow\downarrow$ state. Therefore, $(-K_1/3-K_2/3+K_3+L_1+L_2+L_3-h_x/3)>(L_1+L_2+L_3-h_x/2)$, gives $3K_3>K_1+K_2-1/2h_{1x}$. Finally, since antiferromagnetic ordering is observed for zero field, K_1 must be positive.

Solving these equations yields the following coupling constants:

$$K_1=12.25\ \text{kOe} \quad L_1=-0.5\ \text{kOe}$$
$$K_2=4.5\ \text{kOe} \quad L_2=-1.25\ \text{kOe}$$
$$K_3=2.25\ \text{kOe} \quad L_3=0\ \text{kOe}$$

Figure 10 shows the main features of the phase diagram calculated with these coupling constants is in good qualitative agreement with the measured phase diagram. However, the longer period phases (M_1, M_3, M_4, M_6, and M_9) are absent. In order to obtain the phases with a period greater than six moments, one has to include further ($n>3$) interactions in the spin-chain Hamiltonian, greatly complicating the analysis. It may also be possible to use a more realistic Hamiltonian such as in Ref. 11, where coupling between the $2n$-1 and $2n$ neighbors arise in the nth term of the high-temperature expansion of the free energy. In principle, the introduction of this longer-range coupling may significantly perturb the entire calculated phase diagram, providing the energies are large enough. However, observations of the stability of the calculated phase diagram suggest that the longer-range interactions are quite small. For instance, taking $K_4=0.25$ kOe introduces the M_1 phase ($\uparrow\downarrow\uparrow\downarrow\uparrow\downarrow\uparrow\downarrow\uparrow\downarrow\uparrow$) into the calculated phase diagram, with subsequent shifts of the other coupling constants by the same order of magnitude as K_4. These shifts are an order of magnitude smaller than the original values for the coupling constants, and will only affect the regions in the phase diagram near the present phase boundaries, keeping the main features of the diagram intact. Therefore, for the sake of simplicity we have refrained from considering higher-order interactions.

CONCLUSION

We have shown that the CEF splitting of the Hund's-rule ground state creates a strong anisotropy where the magnetic moment of the Dy^{3+} ions is constrained to one of the $\langle 110\rangle$ orientations within the basal plane. Interactions between the Dy^{3+} ions create a rich system where up to 11 different metamagnetic states become energetically favorable, depending on the magnitude and direction of the applied magnetic field. From the angular dependence of the saturated moments of each state and the critical fields between the states, net distributions of moments may be deduced. Finally, within an extension of the ANNNI model, the ''four-position clock model,'' the coupling constants in the Hamiltonian may be calculated from the triple points in the phase diagram.

Future experiments including high-field magnetic measurements and neutron scattering would be useful to determine the strength of the CEF anisotropy and wave vectors associated with each of the metamagnetic states.

ACKNOWLEDGMENTS

We thank Changyong Song and Zahirul Islam for the determination of sample orientation through x-ray diffraction. Ames Laboratory is operated for the U. S. Department of Energy by Iowa State University under Contract No. W-7405-Eng-82. This work was supported by the Director for Energy Research, Office of Basic Energy Sciences.

[1] P. C. Canfield, S. L. Bud'ko, B. K. Cho, A. Lacerda, D. Farrell, E. Johnston-Halperin, V. A. Kalatsky, and V. L. Pokrovsky, Phys. Rev. B **55**, 970 (1997).

[2] V. A. Kalatsky and V. L. Pokrovsky, Phys. Rev. B **57**, 5485 (1998).

[3] P. C. Canfield and S. L. Bud'ko, J. Alloys Compd. **262-263**, 169 (1997).

[4] S. L. Bud'ko, P. C. Canfield, C. H. Mielke, and A. H. Lacerda, Phys. Rev. B **57**, 13 624 (1998).

[5] R. Wang and H. Steinfink, Inorg. Chem. **6**, 1685 (1967).

[6] F. Hulliger, in *Handbook of Physics and Chemistry of Rare Earths*, edited by K. A. Gschneidner and L. Eyring (North Holland, Amsterdam, 1979), Vol. 4. p. 153.

[7] M. Brylak, M. Möller, and W. Jeitschko, J. Solid State Chem. **115**, 305 (1995).

[8] H. Flandorfer, O. Sologub, C. Godart, K. Hiebl, A. Leithe-Jasper, P. Rogl, and H. Noël, Solid State Commun. **97**, 561 (1996).

[9] O. Sologub, K. Hiebl, P. Rogl, H. Noël, and O. Bodak, J. Alloys Compd. **210**, 153 (1994).

[10] P. C. Canfield and Z. Fisk, Philos. Mag. B **65**, 1117 (1992).

[11] V. L. Pokrovskii and G. V. Uimin, Zh. Eksp. Teor. Fiz. **82**, 1640 (1982) [Sov. Phys. JETP **55**, 5 (1982)].